The impact of pulsed current waveforms on Li dendrite initiation and propagation in solid-state Li batteries

V. Reisecker[a,b#], F. Flatscher[b,c#], L. Porz[c], C. Fincher[d], I. Hanghofer[e], V. Hennige[e], M. Linares-Moreau[f], P. Falcaro[f], S. Ganschow[g], S. Wenner[h], Y.M. Chiang[d], J. Fleig[i], D. Rettenwander[a,b,c*]

[a] Institute of Chemistry and Technology of Materials, Graz University of Technology, Graz, Austria.
[b] Christian Doppler Laboratory for Solid-State Batteries, NTNU Norwegian University of Science and Technology, Trondheim, Norway.
[c] Department of Material Science and Engineering, NTNU Norwegian University of Science and Technology, Trondheim, Norway.
[d] Department of Materials Science & Engineering, Massachusetts Institute of Technology, Cambridge, MA, USA
[e] AVL List GmbH, Graz, Austria
[f] Institute of Physical and Theoretical Chemistry, Graz University of Technology, Graz, Austria
[g] Leibniz-Institut für Kristallzüchtung, Berlin, Germany
[h] Sintef Industry, Department of Materials and Nanotechnology, Trondheim, Norway
[i] Institute of Chemical Technologies and Analytics, TU Wien, Vienna, Austria

[#]Authors, V. Reisecker and F. Flatscher, equally contributed to this work.
[*]Corresponding author: daniel.rettenwander@ntnu.no

Lithium dendrites are amongst the key challenges hindering Solid-State Li Batteries (SSLB) from reaching their full potential in terms of energy and power density. The formation and growth of these dendrites cause an inevitable failure at charge rates far below the threshold set by industry (>5 mA/cm^2) and are supposedly caused by stress accumulation stemming from the deposited lithium itself. Herein, we demonstrate that MHz pulsed currents can be used to increase the current density by a factor of six, reaching values as high as 6.6 mA/cm^2 without forming Li dendrites. To understand the origin of this improvement we propose an extension of previous mechanisms by considering the Li activity as a critical factor. The Li activity becomes relevant when Li is geometrically constrained, and the local plating rate exceeds the exchange current density. Over a critical Li activity, the solid-state electrolyte close to the tip of the dendrite fractures and releases the accumulated elastic energy. These events deteriorate the functional and mechanical performance of the SSLB. Since the buildup of a critical Li activity requires a certain time, the application of current pulses at shorter time scales can be used to significantly improve the rate-performance of SSLB, representing a potential step towards the practical realization of electric vehicles and other emerging applications.

Introduction

Li-Ion Batteries (LIBs) are considered to be one of the key technologies to guide our society into a more sustainable and emission-free future. However, conventional LIBs have almost reached their limit in terms of energy densities (~250 Wh/kg)[1,2], which are not sufficient to meet the requirements and demands of future electric vehicles (the required energy density is envisioned to be above 400 Wh/kg).[3] To achieve such high performance targets, novel energy storage solutions such as Solid-State Batteries using Li-metal anodes (SSLB) in combination with high-capacity (e.g. S) or high-voltage (e.g. layered-structure $LiNi_{0.8}Co_{0.1}Mn_{0.1}O_2$) cathodes, separated by a Solid-State Electrolyte (SSE), are crucial to enable energy densities up to 500 Wh/kg.[3,4] One of the most promising candidates to be used as SSE is $Li_7La_3Zr_2O_{12}$ (LLZO) due to its (i) room-temperature Li-ion conductivity approaching that of liquid electrolytes, and (ii) excellent chemical and electrochemical stability towards Li metal and high voltage cathodes.[5]

However, to reach the promised performance, SSLBs must plate a large Li thickness (at least 15 µm or 3 mAh/cm^2) at a high (charging) current rate (>5 mA/cm^2) for a minimum of 1000 full cycles[6-9] Today, under such conditions, SSLBs invariably fail due to the formation of Li dendrites penetrating the SSEs and causing a short-cicuit.[10] One of the main reasons for this battery failure are current constrictions at the Li|SSE interface that arise from, e.g., (i) poor contact between the Li metal electrode and the SSE, (ii) grain boundaries, or (iii) void formation at the Li|SSE interface during Li metal stripping.[6,7] The resulting high local current densities lead to electro-chemo mechanical stresses high enough to initiate Li penetration into the SSE, finally resulting in a short circuit and even catastrophic cell failure. [6,8-10]

Pulsed currents are often utilized in electroplating of metals to achieve uniform morphologies, and therefore represent a potentially useful method for inhibiting Li dendrite formation.[11] In conventional LiBs upon current application, Li ions start to deposit throughout the whole electrode|electrolyte interface and can gather in certain areas causing concentration gradients. During the pausing times, the Li ions then diffuse from regions of high concentrations towards regions of low concentrations, resulting in a dense uniform Li-ion deposition.[12,13] For example, the Li morphologies for different current waveforms in a Li-LiFePO$_4$ battery using a liquid electrolyte have been studied by Grecia, et al.[14] They found that the application of current pulses leads to dense microstructures, whereby a conventional DC current initiates rapid growth of porous Li film structures, degrading the cycling performance significantly.[14] Moreover, it has been shown that the mitigation of current constrictions by pulsed current waveforms enables suppression of the dendrites growth by 96 %.[11,15,16]
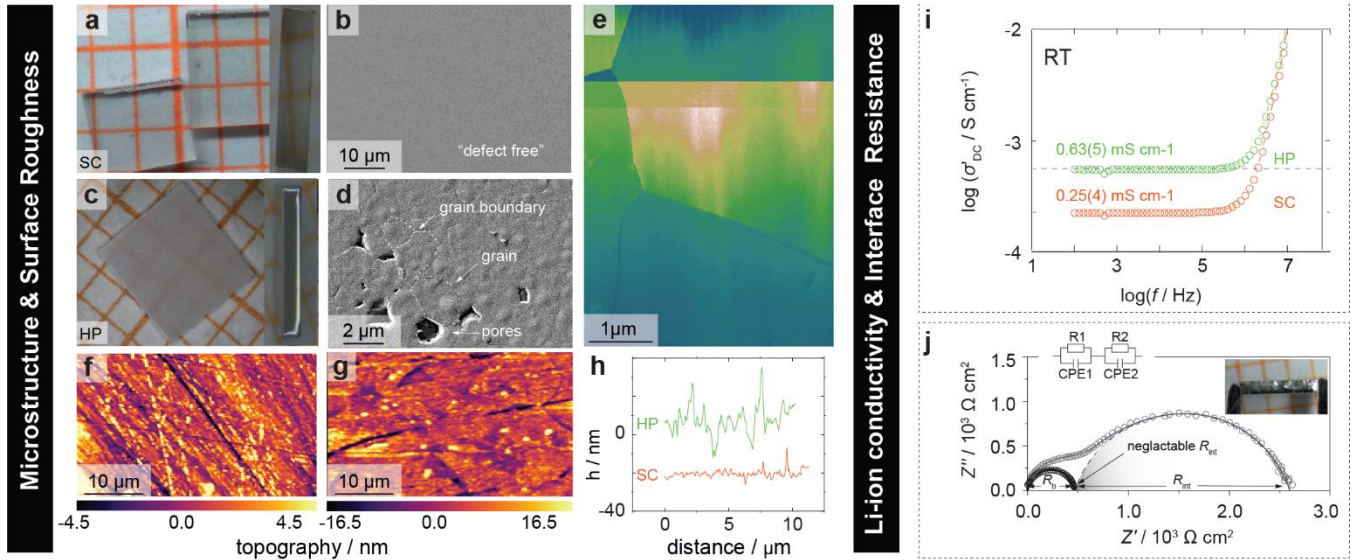
Fig. 1. Design and characterization of testing platform. (a) Single-Crystalline $Li_6La_3ZrTaO_{12}$ (SC) and (c) Hot-Pressed $Li_{6.4}La_3Zr_{1.4}Ta_{0.6}O_{12}$ (HP) in top and side view after shaping and thorough polishing. The samples were additionally investigated via SEM (b SC, d HP) prior to coating with Li:Sn, whereas the HP sample was additionally examined via TEM (e). In the case of the SC no indication of any microstructural defect was found, whereas the HP shows a very dense microstructure composed of grains with diameters around 2 μm and pores up to 1.5 μm. Corresponding AFM analysis was conducted to assess the defect concentration of the SC (g) and HP (h) surface and the measured height profile plotted against the distance covered (i). Note: for comparison reasons the AFM topography profile of the SC was shifted by -20 nm. (j) Conductivity isotherm of SC and HP measured in a symmetrical Li cell at room temperature (RT). (k) Nyquist plot of an SC with (black) and without (grey) a proper surface treatment, measured in a symmetrical Li cell at RT without stack pressure.

Despite the potential of pulse plating to surmount the limitation imposed by Li dendrites in conventional LiBs, its effectiveness with respect to SSLB has received only minor attention. Specifically, it is not clear to which extent and how pulsed current waveforms can increase the Critical Current Density (CCD) of SSLBs.

Therefore, Single-Crystalline $Li_6La_3ZrTaO_{12}$ (SC) and Hot-Pressed poly-crystalline $Li_{6.4}La_3Zr_{1.4}Ta_{0.6}O_{12}$ (HP) cuboids of high geometrical and interfacial quality were prepared and subjected to different pulse plating protocols. A wide spectrum of techniques, such as Focused Ion Beam (FIB), Secondary Electron Microscopy (SEM), Transmission Electron Microscopy (TEM), Atomic Force Microscopy (AFM) and Electrochemical Impedance Spectroscopy (EIS), were applied to retrieve a full sample profile. Afterwards, all samples were galvanostatically cycled in symmetrical Li cells using either direct or pulsed current operation, whereby short circuits have been identified and tracked via operando Optical Microscopy (OM).

This study reveals that MHz pulses enable up to a six-fold increase in CCD, leading to values as high as 6.6 mA/cm². The increase in CCD can be associated with the application of current pulses shorter than the time required to build up a critical Li activity near the defect tip. This critical Li activity leads to the structural destabilization and fracture of the SSE, which is accompanied by Li dendrite initiation and propagation.

Results & Discussion

Ensure minimum sample-to-sample variation. One of the main challenges in studying the CCD in a reliable and reproducible manner is its dependency on microstructural features like grain boundaries, voids and flaws[17,18] or also mechanical variations even within similarly prepared samples.[19,20] In order to reduce the impact of sample-specific parameters on the CCD measurements and guarantee comparable starting conditions for all experiments, special attention was paid to minimize sample-to-sample variations for each morphology type. Therefore, rectangularly shaped SC and HP samples exhibiting similar sizes of roughly 3 mm × 3 mm × 0.5 mm with densities of 100 % and >99 %, respectively, were prepared (Fig. 1a,c, details regarding the sample preparation can be found in Supplementary Section 1 as well as Supplementary Fig. 1-2). To achieve a minimal defect concentration at the SSE surface, a thorough surface treatment procedure consisting of multiple rotational and vibrational polishing steps was applied. SEM images of the SCs did not reveal any macroscopic pores or larger scratches (Fig. 1b) present at the polished surface. The HP samples showed a dense microstructure with grains in the size of about 4 μm in diameter (Fig. 1d,e) and only minor pores up to about 1 μm in diameter (Fig. 1d). In both cases, a smooth surface profile was achieved with Root Mean Square (RMS) roughness values of 2.9(2) nm and 7.7(3) nm for the SC and HP samples, respectively (Fig. 1f,g).

Besides its morphological dependency, the CCD has been found to be heavily influenced by current constrictions along the Li|SSE interface.[6,7] Current constrictions are related to missing contact associated with, e.g., insufficient Li wetting or surface contaminants.
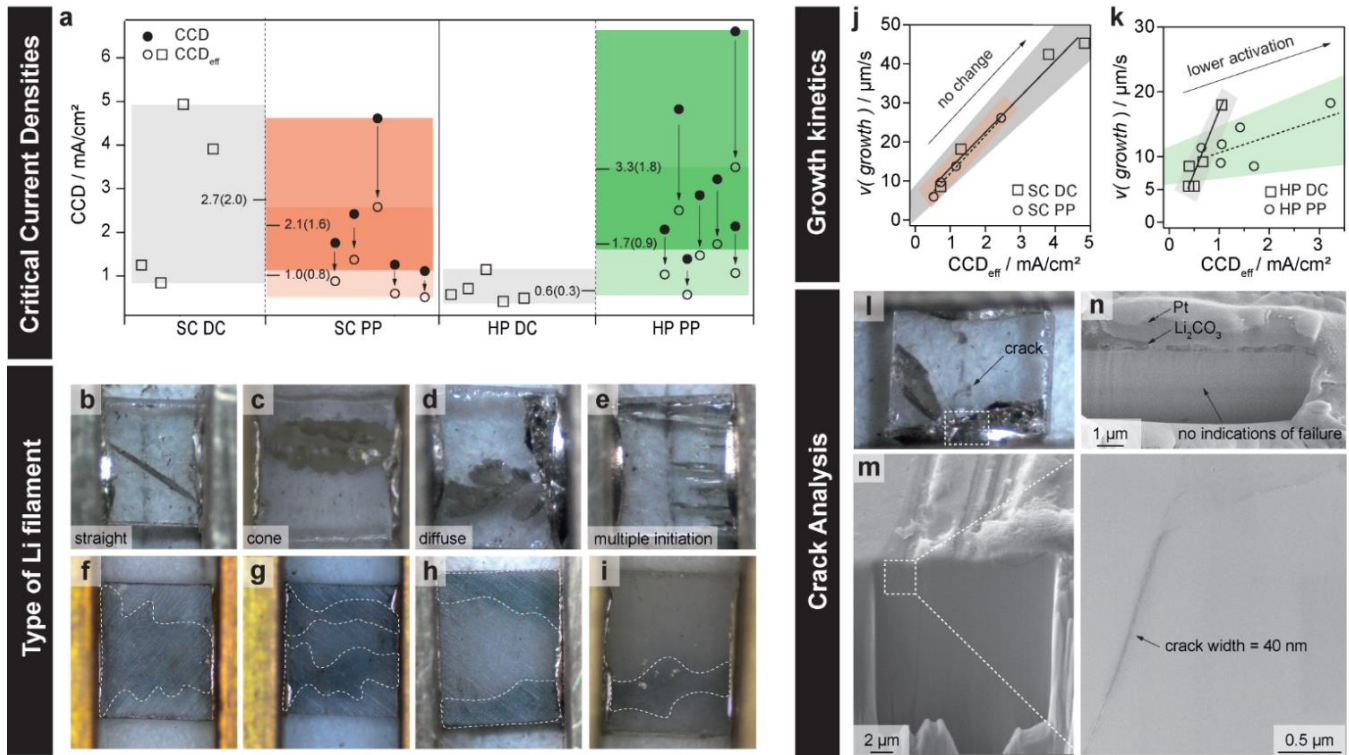
Fig. 2. **Electrochemical and visual characterization.** (a) Ranking of the CCD values achieved by SC and HP samples during either DC (marked in grey) or PP (marked in orange and green for SC and HP, respectively) operation. CCD values obtained during PP are shown in black, whereas effective CCD values, considering the time increase during the measurement compared to the DC values, are plotted in white. Overview of different Li dendrites observed during optical tracking of SC samples being of either straight (b), cone (c) or diffuse (d) type. In some cases, multiple dendrite initiation (e) was spotted. HP showed Li deposition throughout larger areas of the SSE (f-i). Growth rates plotted against the CCD values for both LLZTO systems in case of DC or PP operation (j,k) along with a crack analysis performed via SEM for an SC (l-m) and an HP (n).

Moreover, the ratio between the conductivity of the SSE and the exchange current density has been shown to have a significant impact on the uniformity of metal deposits.[21] The Area Specific Resistance (ASR) directly reflects both, the exchange current density (according to Butler-Volmer) and the degree of physical contact[6]. Hence, a reliable experimental platform has to ensure similar ASR values, as well as similar Li-ion conductivities within one experiment series. Therefore, potential contaminants at the SSE surface, such as LiOH and Li_2CO_3, have been removed by a proper polishing sequence with a subsequent heat treatment at 400 °C in Ar atmosphere, according to Ref. [22]. Moreover, a molten Li:Sn electrode (70:30 wt%) has been used to improve the wetting of Li on the SSE, according to Ref. [23]. The combination of both approaches led to a reproducible reduction of the ASR value down to negligible values (see Figure 1j). This is elaborated further in Supplementary Tab. 1 and 2 as well as Supplementary Fig. 3. The variation in Li-ion conductivity across the SC and HP samples was investigated by plotting the EIS data in a Bode-like fashion (Fig. 1i). Both conductivity isotherms reveal a single DC plateau, which, in the case of the SC, can be related to the bulk conductivity due to the lack of grain boundaries. In case of the HP sample, the grain boundaries appear to not significantly contribute to the total resistance of the SSE, resulting in a single contribution as well. The averaged

conductivities and deviations of the SC and HP samples amount to 0.25(4) mS/cm and 0.63(5) mS/cm, respectively, pointing towards minor sample-to-sample variations in terms of resistance. Additional information can be found in Supplementary Fig. 5 and 6.

In addition to these parameters, experimental conditions, like temperature[24] and pressure[25], greatly impact the CCD. Increasing either temperature and/or pressure can significantly elevate the CCD value, e.g., by enhancing the creep of Li metal and its diffusivity, which is why all experiments were conducted at a constant temperature (21(1) °C) and without the application of stack pressure.[24,25]

The critical current density. Different pulsing sequences were tested in preliminary experiments with poly-crystalline LLZTO (PC) pellets prepared by conventional solid-state synthesis (see Supplementary section 1), where the pulse-pause ratio was varied from 1:1 to 1:10 in the ms-range. Whereas these cycling conditions did not improve the electrochemical performance of the PC pellets, reducing the respective timeframes to the μs-regime greatly enhanced the CCD values achieved in contrast to DC operation for a 1:1 pulse plating (PP) condition (see Supplementary Tab. 2). The same pulsing sequence was then applied to the SC and HP samples and compared to the CCD values achieved under DC operation (see Fig. 2a and Supplementary Tab. 3 and 4). Since the

pausing time in the pulsing sequence prolongs the overall cycling time, an "effective" CCD value (CCD$_{eff}$) was defined on the basis of the plated capacity for better comparison. For a 1:1 pulsing sequence, taking twice as long as DC cycling, the obtained CCD value was therefore divided by two. Prior to any cycling experiment conducted with pulsed waveforms, the efficiency was evaluated by galvanostatic titration and plating experiments. The measurements revealed that PP down to the µs-range can achieve efficiencies up to 100 % (see Supplementary Fig. 7 and 8). In the case of the SC and HP samples, the cycling profile was complemented by simultaneously taken OM images, easing the identification of Li dendrite formation (details are given in Supplementary Fig. 9, 10 and the Supplementary Vid.).

For the SC samples, CCD values up to 5 mA/cm² have been achieved by using DC. Compared to similar samples lacking an extensive surface treatment[9], this represents an increase of around 170 %, thereby highlighting the sensitivity of the CCD on the SSE's surface condition. In Fig. 3a and in Supplementary Tab. 5 previously reported CCD values are summarized (note: based on the effective surface area; values related to potential soft shorts, higher temperature and high stack pressure are excluded). Values up to 4 mA/cm² have so far been achieved by using alloys (e.g. Li:Mo, Sr:Li), additives (e.g. LiOH.H$_2$O) and/or interface engineering (e.g. MgO, Cu-doped Li$_3$Zn).[26-41] While the SC samples exceed these values by 1 mA/cm², they are, however, not practicable for future devices, due to cost and time of manufacturing. Applying a DC program to the HP samples, however, led to average CCD values below 1 mA/cm², proving that the presence of grain boundaries and small pores significantly reduces the CCD (see Supplementary Tab. 3 and 4). When switching to PP, no significant difference in electrochemical performance could be found for the SC samples. While the maximum CCD reached a similarly high value of 4.8 mA/cm², the overall average was lower, taking on a value of 2.1(1.6) mA/cm², as opposed to 2.7(2.0) for DC cycling. Based on the CCD$_{eff}$ of 1.0(0.8) mA/cm² it becomes evident that in the case of SCs, PP cannot effectively enhance the CCD. For HP samples on the other hand, a superior improvement could be observed with a maximum CCD of 6.6 mA/cm² and an average of 3.3 (1.8) mA/cm². Even based on the CCD$_{eff}$ of 1.7(0.9) mA/cm², PP can by far outperform cells cycled under DC conditions reaching average CCDs around 0.6(0.3) mA/cm².

These results suggest that MHz pulsed currents can mitigate critical defects up to a certain current density range, enabling CCDs as high as 6.6 mA/cm², and an increase by a factor of three concerning the plated capacity. Notably, despite our efforts to mitigate as many influencing factors as possible, large variations in CCD values were still observed. This suggests that studies on CCDs should, in general, be statistically evaluated to ensure reproducibility.

Li dendrite characteristics. During optical tracking of Li dendrite initiation and propagation in SCs, a multitude of differen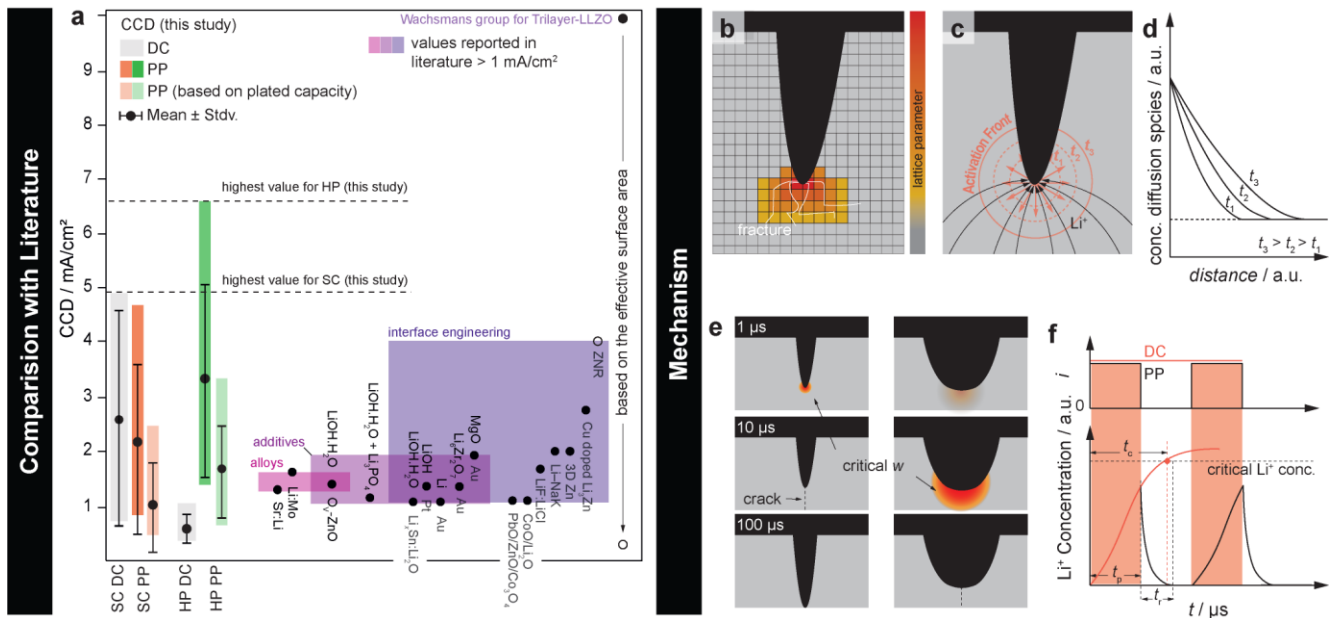t dendrites has been observed, which were essentially grouped into one of three different categories according to the classification used by Kazyak, *et al.*[42]: straight, cone or diffuse type. The straight type (Fig. 2b) is characterized by a 2D Li deposition throughout the SSE, whereas the cone type (Fig. 2c) branches out at the sides causing more of a 3D growth pattern. In the case of the diffuse type (Fig. 2d), Li did plate in a flowing manner followed by a macroscopic fracture of the SSE. Fig. 2k-m shows the analysis of the crack widths of a typical shorted sample using FIB-SEM. In the SC sample cracks with widths of about 40 nm were observed, whereas the HP sample did not show any signs of intra- and/or intergranular crack propagation. This observation could, however, also be related to the formation of dendrites below the resolution limit of the SEM. As all dendrite types were observed in both cycling programs, no clear correlation between the current waveform and the respective shape of the dendrite could be found. In most cases, either a straight or cone-like Li propagation was observed, whereas the diffuse type was encountered very rarely. In contrast to the observations Kazyak, *et al.*[42] have made, the propagation of each dendrite type was accompanied by a decrease in potential. Overall, initiation sites were found to be randomly distributed across the whole interface and only numerous in case of high CCD values (Fig. 2e). As for the HP samples, Li dendrite formation was not observed to follow a single initiation event, but multiple ones, starting simultaneously throughout larger areas of the Li|SSE interface (Fig. 2f-i). Next to so-called hard shorts, soft shorts exhibiting reversible Li deposition have also been observed but were not further studied herein (see Supplementary Fig. 11 and 12).

The growth kinetics. Growth rates were determined by the distance between the electrodes divided by the time needed to reach the opposing electrode. Fig. 2j,k show the average growth rates of both morphology types obtained under either DC or PP conditions. A linear relationship between the CCD and the growth rate becomes evident, which is in agreement with previous studies.[42] In the case of the SCs, Li deposition rates as a function of CCD progressed at speeds of 8.4 µm/(s (mA/cm²)) and 10.5 µm/(s (mA/cm²)) under DC and PP operation, respectively, indicating little dependence of the Li deposition mechanism on the pulse waveform. Applying the same approach to the HPs, PP was observed to significantly reduce the growth rate increase with CCD of Li from 13.7 µm/(s (mA/cm²)) to 1.1 µm/(s(mA/cm²)). These observations suggest that Li propagation follows a different mechanism in poly-crystalline samples under pulsed currents as opposed to in single-crystalline ones.

The growth rate of a dendrite can be expressed by dx/dt and based on our observation takes on a value of about 10 µm/s at 1 mA/cm². The current density at the tip required to enable growth rates up to 10 µm/s can be derived from Eq. 1.

$$j = \frac{I}{A} = \frac{\left(\frac{dV}{dt} * \frac{1}{V_m^{Li}}\right) * F}{A} = \frac{\left(A * \frac{dx}{dt} * \frac{1}{V_m^{Li}}\right) * F}{A} = 7 \frac{A}{cm^2} \qquad \text{Eq. 1}$$

Fig. 3. **Comparison with literature and proposed mechanism.** (a) CCD values obtained for SC and HP samples cycled via direct (grey) and pulsed currents (orange/green) herein as well as CCD values above 1 mA/cm² reported in literature so far for different LLZO chemistries (excluding potentially soft shorted samples or values obtained at temperature higher than RT and/or high stack pressure, to our best knowledge; based on Ref. [26-41] from left to right). Values were grouped into one of three categories depending on their success recipe being either the coating of an alloy onto the SSE, application of an additive during the sintering procedure or the engineering of the SSE interface by e.g. structuring or application of an additional interlayer. (b) In case the Li-activity reaches a critical Li concentration, LLZO will structurally degrade, causing crack formation which in turn accelerates dendrite initiation and growth. (c) Li filled defect where the flux of Li-ions approaching the tip (black arrows) exceeds the Li-ion flux away from the tip (orange arrows), leading to a significant increase in Li-activity near the tip. (d) Diffusion front at SSE|Li interface and growth of rim with increasing time (c). (e) Schematics illustrate that a smaller activity front is sufficient to crack up the environment of small defects whereas a thicker activity front is needed for the same result in case of bigger defects. It therefore takes for a longer time to induce fracture in the vicinity of big defects as opposed to smaller ones. (f) Increase of Li concentration as a function of plating time. The illustration shows that if the current is applied for a shorter amount of time than what is needed to reach the critical Li concentration, a structural degradation can be avoided/delayed.

The total current flowing is denoted by I, the molar volume by V_m^{Li}, which amounts to 13.148 cm³/mol an F represents the Faraday constant. Note that the tip area of the dendrite A cancels out in the equation, which means that the current density is independent of the size of the dendrite in a first approximation. As long as the current for the entire cell is much larger than the current needed for driving the dendrite, which is typically the case evidenced by no or only minor voltage drops before a short circuit, such an approximation can be made. According to this relation, the current densities needed to achieve the observed growth rates are in the range of 7 A/cm² when considering the required charge transfer to provide the necessary volume of Li. This value is significantly larger than the exchange current densities reported for LLZO so far, which lie around 50 mA/cm².[6] Hence, the high current density causes a significant polarization at the dendrite tip during plating with detrimental consequences as outlined below.

The mechanism. The propagation of dendrites through ceramic electrolytes is suggested to be associated with the geometrical constraint for Li within a defect. Due to this constraint, a critical pressure builds up as soon as the defect is filled, causing a protrusion of Li into the SSE. This

failure occurs instantaneously with the applied current (see finite element calculation in Supplementary Fig. 13 and 14). Consequently, due to the significantly longer pulse duration compared to the instantaneous build-up of stress, pulse plating should not have any implications on the propagation of Li dendrites. The experiments with the HP samples, however, showed that the CCD is increased by a factor of six, whereas the Li growth rate decreases by one order of magnitude when switching from DC to PP. Hence, the previously proposed mechanism of mechanical failure associated with the penetration of Li needs to be revisited to describe our observations. Our main hypothesis is, that the occurrence of Li dendrites is associated with the fracture of the SSE in the next-proximity of the defect tip, caused by the buildup of a Li-activity front, which can be, however, mitigated if the pulse length is shorter than the time constant to reach a critical Li-activity.

We must consider that bonds need to be broken in order to extend cracks within an SSE to allow the propagation of Li dendrites. In this case the corresponding driving force is, however, introduced locally and not as approximated previously by a homogeneous load[7]. The required energy gain to overcompensate the energy needed to break bonds comes from (i) the release of the chemical driving force

evoked by a Li chemical potential (or activity) in the SSE being above that of Li metal, and (ii) the release of the elastic energy due to an enhanced Li activity in SSEs around the dendrite (and crack) tip. Both energy contributions emerge from the same phenomenon, being the accumulation of Li ions and electrons in close proximity to the Li-filled crack tip once an electrode overpotential is applied. This is in accordance with Han *et al* where a substantial enhancement of the electronic conductivity is found close to the Li electrode upon polarization.[43] In Solid State Ionics this is well known as stoichiometry polarization or Wagner-Hebb polarization, where a blocking of ionic charge carriers at the electrode is present [44,45] This is valid, as long as the critical conditions leading to the initiation and growth of Li dendrites are not met. Then, LLZO is locally reduced and thus the electron concentration enhanced, driven by the extreme current densities of beyond 1 A/cm² (see above). The local stoichiometry change (i.e., additional Li-ions and changed ionic valences due to additional electrons) induces a change of the local lattice parameter similar to, e.g., doped ceria (i.e., SSE for solid oxide fuel cells) under very reducing conditions,[46] This change only arises near the defect-tip region and is therefore suppressed by the mechanical constraints towards the bulk part of LLZO, which is unaffected by Li activity changes. Accordingly, a substantial elastic energy builds up, until a critical Li activity is reached resulting in stress relaxation by fracture (Fig. 3b).[,47] Similar behavior can be found, e.g., for LiCoO$_2$,[48] and Si[49] where the insertion of Li ions into the particle causes a volume mismatch between the new phase near the surface and the existing phase in the bulk once the relaxation kinetics is slower than the transfer rate. This volume mismatch causes a high enough chemo-mechanical strain to induce plastic deformation, mechanical fracturing and even amorphization. In nature this effect can be found in, e.g., fracture of rock formations as a consequence of water uptake, which could be seen as an analogous mechanism. The change of the unit cell upon incorporation leads to an expansion or shrinkage, inducing stresses which eventually cause the stone to crack.[50]

In contrast to previously proposed mechanisms, e.g., Porz *et al*[7] or Han *et al*[43], this implies that dendrite propagation is promoted by the mechanical weakening of the SSE (i.e., decrease of the fracture resistance) at the crack tip caused by the constant increase in Li activity under current application. The time dependence of this process can be described by the ambipolar (chemical) diffusion coefficient of Li ions in LLZO. The exact time and space thereby depend on the geometry of the defect and the location at which Li-ions are injected and where electrons originate from.[51] The increase in Li activity takes place at the Li|LLZO interface (Fig. 3c), whereby in a first approximation a few assumptions can be made. On the one hand that there is an equilibration of electrons and on the other hand that any change of the interfacial double layer and any additional contribution of the interfacial charge transfer to the kinetics (i.e., considering diffusion rather

than the Butler-Volmer limited case) can be neglected. Hence, the applied overpotential directly transfers to a locally enhanced Li activity creating an activity front at the Li dendrite tip. The diffusion into the surrounding LLZO regions (Fig. 3c,d), is determined by the chemical diffusion coefficient of Li ions, D. Assuming radial symmetry for diffusion, a constant D value and concentrations instead of activities, the additional Li-ion concentration $C(r)$ in the corresponding region can be determined with Eq. 3.

$$C(r) = C(R) \cdot erf\sqrt{r/Dt} \qquad \text{Eq. 3}$$

The quantitative relation between the additional Li-ion concentration and the activity of Li (or the overpotential) is not known. However, the effective thickness w of such a diffusion front can be approximated according to Eq.4.

$$w = \sqrt{Dt} \qquad \text{Eq. 4}$$

It shows that this „rim", having an enhanced Li activity, increases with time (Fig. 3d). From a mechanistic point of view, the tip radius defines the stress concentration at a flaw. We suppose that to reach the critical condition for dendrite growth, a certain Li activity is needed at the tip. For example, based on Eq. 4, it will take 100 times longer to reach critical conditions for a ten times larger R (see Fig. 3e). Therefore, a tip with a large radius R (e.g., pores, scratches) requires a thicker activity front as opposed to a sharp tip (e.g., grain boundaries). In other words, the time required to reach the critical activity front is shorter for a tip with smaller R. Since the accumulation of a critical activity front at a dendrite takes place in the sub-ms range (depending on the applied current), this time dependence does not play a significant role for DC charging.

In the case of PP however, this time dependence becomes significant. For 1 MHz pulses the activity front can build up for just one microsecond, which is too short to reach critical conditions. In the subsequent microsecond the Li activity front can then relax again during the pausing time (Fig. 3f). Hence, the propagation of Li dendrites is suppressed by taking away the driving force, i.e., fracture of the SSE at high Li activity. This explains the increase in CCDs and lower propagation rates of Li dendrites in case of the HP samples when PP is applied and why the SC samples remain unaffected under the same conditions. Considering that grain boundaries are sharp defects with lower fracture toughness compared to the bulk, Li dendrites are predominantly formed in these regions (see detailed discussion on the failure likeliness of different types of defects and defect sizes in Supplementary Fig. 15). Hence, when the pulsed current frequency is sufficiently high, Li penetration will then take place, e.g., along grain boundaries at much higher currents (or any other defect for which the time required to reach a critical Li activity front is less than the pulse frequency) explaining the six-fold increased CCD for HP. The lower propagation rate during pulsed current application can be associated with local fluctuations in Li-ion transport and Li deposition rates.[43] These cause stress accumulation at the branch tips,

which are created once Li starts to penetrate the SSE. Considering that the branch tips are "sharper", as opposed to the primary tip, they are most sensitive to failure (see above). Consequently, dendrites under pulsed conditions must pass a longer pathway, hence, require more time until a short-circuit occurs. Due to the absence of grain boundaries, SCs naturally short at higher CCD values approaching those of HP under PP conditions. At these current densities, however, 1 MHz pulses are not sufficient anymore to mitigate the build-up of a critical activation front, keeping the CCD unaffected by pulsing. Hence, PP appears to be particularly powerful for improving the behavior of industrially relevant polycrystals.

Conclusion

To this date, lithium dendrites appear to be the Achilles' heel of SSLBs and hinder their implementation in energy intensive applications. [1,2] In order to overcome the CCD barriers set by the automotive branch (>5 mA/cm2) and become a competitive option for electric vehicles, novel strategies are needed to exceed this limitation. Herein, we demonstrate that the application of MHz-pulsed currents increases the CCD by a factor of six, leading to values as high as 6.6 mA/cm² exceeding values reported in literature so far. To understand the origin of this improvement, the preexisting mechanism of Li dendrite formation must be extended. We propose that an enhanced Li activity close to the filament tip arises once Li deposition within a defect is limited by geometrical constraints, which, in turn, causes the effective current density at the crack tip to exceed the exchange current density. The increase in Li activity is accompanied by a lattice expansion that is constrained towards the bulk causing a buildup of elastic energy. Once a critical current has been reached, this energy is released by fracture of the ceramics. Since the buildup of a critical Li activity requires a certain time, the application of current pulses with shorter durations can be used to extend the stability range of the SSE, and therefore increase the achievable CCD. We propose that a combination of pulsed current waveforms with other established methodologies, like the application of interlayers or increased interfacial surface areas, can boost the performance of SSLB to enable future EVs with wider driving range as well as improved safety.

DATA AVAILABILITY
The datasets generated during and/or analyzed during the current study are available from the corresponding author on reasonable request.

REFERENCES

1. Liu, Jun, et al. *Pathways for practical high-energy long-cycling lithium metal batteries.* Nat. Energy **4** (2019) 180-186.
2. Shen, Yanbin, et al. *Unlocking the energy capabilities of lithium metal electrode with solid-state electrolytes.* Joule **2.9** (2018): 1674-1689.
3. Judez, Xabier, et al. *Opportunities for rechargeable solid-state batteries based on Li-intercalation cathodes.* Joule **2** (2018): 2208-2224.
4. Albertus, Paul, et al. *Status and challenges in enabling the lithium metal electrode for high-energy and low-cost rechargeable batteries.* Nat. Energy **3.1** (2018): 16-21.
5. Murugan, Ramaswamy, Venkataraman Thangadurai, and Werner Weppner. *Fast lithium ion conduction in garnet-type $Li_7La_3Zr_2O_{12}$.* Angew. Chem. Int. Ed. **46** (2007): 7778-7781.
6. Krauskopf, Thorben, et al. *Toward a fundamental understanding of the lithium metal anode in solid-state batteries—an electrochemo-mechanical study on the garnet-type solid electrolyte $Li_{6.25}Al_{0.25}La_3Zr_2O_{12}$.* ACS Appl. Mater. interfaces **11** (2019): 14463-14477.
7. Kasemchainan, Jitti, et al. *Critical stripping current leads to dendrite formation on plating in lithium anode solid electrolyte cells.* Nat. Mater. **18.10** (2019): 1105-1111.
8. Krauskopf, Thorben, et al. *Lithium-metal growth kinetics on LLZO garnet-type solid electrolytes.* Joule **3.8** (2019): 2030-2049.
9. Neudecker, B. J., N. J. Dudney, and J. B. Bates. *"Lithium-Free" Thin-Film Battery with In Situ Plated Li Anode.* J. Electrochem. Soc. **147.2** (2000): 517.
10. Lu, Dongping, et al. *Failure mechanism for fast-charged lithium metal batteries with liquid electrolytes.* Adv. Energy Mater. **5.3** (2015): 1400993.
11. Yang, Heng, et al. *Effects of pulse plating on lithium electrodeposition, morphology and cycling efficiency.* J. Power Sources **272** (2014): 900-908.
12. Sun, Xiaowen, et al. *Revisiting the Electroplating Process for Lithium-Metal Anodes for Lithium-Metal Batteries.* Angew. Chem. Int. Ed. **59.17** (2020): 6665-6674.
13. Aryanfar, Asghar, et al. *Dynamics of lithium dendrite growth and inhibition: Pulse charging experiments and Monte Carlo calculations.* J. Phys Chem **5.10** (2014): 1721-1726.
14. García, Grecia, et al. *Exceeding 6500 cycles for LiFePO4/Li metal batteries through understanding pulsed charging protocols.* J. Mater. Chem. A **6.11** (2018): 4746-4751.
15. Schneider, Nicholas M., et al. *Nanoscale evolution of interface morphology during electrodeposition.* Nat. Commun. **8.1** (2017): 1-10.
16. Qu, Z. G., Z. Y. Jiang, and Qiong Wang. *Experimental study on pulse self–heating of lithium–ion battery at low temperature.* Int. J. Heat Mass Transf. **135** (2019): 696-705.
17. Porz, Lukas, et al. *Mechanism of lithium metal penetration through inorganic solid electrolytes.* Adv. Energy Mater. **7.20** (2017): 1701003.
18. Swamy, Tushar, et al. *Lithium metal penetration induced by electrodeposition through solid electrolytes: example in single-crystal $Li_6La_3ZrTaO_{12}$ garnet.* J. Electrochem. Soc. **165.16** (2018): A3648.
19. Wachter-Welzl, A., et al. *The origin of conductivity variations in Al-stabilized $Li_7La_3Zr_2O_{12}$ ceramics.* Solid State Ion. **319** (2018): 203-208.
20. Wachter-Welzl, Andreas, et al. *Microelectrodes for local conductivity and degradation measurements on Al stabilized Li7La3Zr2O12 garnets.* J. Electroceramics **38.2** (2017): 176-181.
21. Cheng, Lei, et al. *Effect of surface microstructure on electrochemical performance of garnet solid electrolytes.* ACS applied materials & interfaces **7.3** (2015): 2073-2081.
22. Sharafi, Asma, et al. *Surface chemistry mechanism of ultra-low interfacial resistance in the solid-state electrolyte $Li_7La_3Zr_2O_{12}$.* Chem. Mater. **29.18** (2017): 7961-7968.
23. Wang, Chengwei, et al. *Universal soldering of lithium and sodium alloys on various substrates for batteries.* Adv. Energy Mater. **8.6** (2018): 1701963.
24. Wang, Michael, Jeffrey B. Wolfenstine, and Jeff Sakamoto. *Temperature dependent flux balance of the Li/Li7La3Zr2O12 interface.* Electrochim. Acta **296** (2019): 842-847.
25. Wang, Michael J., Rishav Choudhury, and Jeff Sakamoto. *Characterizing the Li-solid-electrolyte interface dynamics as a function of stack pressure and current density.* Joule **3.9** (2019):

2165-2178.

26. He, Xinzi, et al. *Tuning Interface Lithiophobicity for Lithium Metal Solid-State Batteries.* ACS Energy Letters **7.1** (2021): 131-139.

27. Wei, Ying, et al. *An oxygen vacancy-rich ZnO layer on garnet electrolyte enables dendrite-free solid state lithium metal batteries.* Chem. Eng. J.**433** (2022): 133665.

28. Yang, Li, et al. *Rapid preparation and performances of garnet electrolyte with sintering aids for solid-state Li–S battery.* Ceram **47.13** (2021): 18196-18204.

29. Chen, Yue, et al. *Nanocomposite intermediate layers formed by conversion reaction of SnO_2 for Li/garnet/Li cycle stability* J. Power Sources **420** (2019): 15-21.

30. Liao, Yu-Kai, et al. *Extensively Reducing Interfacial Resistance by the Ultrathin Pt Layer between the Garnet-Type Solid-State Electrolyte and Li–Metal Anode.* ACS Appl. Mater. Interfaces **13.47** (2021): 56181-56190.

31. Huang, Xiao, et al. *None-mother-powder method to prepare dense Li-garnet solid electrolytes with high critical current density.* ACS Appl. Energy Mater. **1.10** (2018): 5355-5365.

32. Zheng, Chujun, et al. *Grain boundary modification in garnet electrolyte to suppress lithium dendrite growth.* Chem. Eng. J. **411** (2021): 128508.

33. Guo, Haojie, et al. *Achieving high critical current density in Ta-doped $Li_7La_3Zr_2O_{12}$/MgO composite electrolytes.* J. Alloys Compd. **856** (2021): 157222.

34. Cai, Mingli, et al. *Robust Conversion-Type Li/Garnet interphases from metal salt solutions.* Chem. Eng. J. **417** (2021): 129158.

35. Lu, Guanjie, et al. *Universal lithiophilic interfacial layers towards dendrite-free lithium anodes for solid-state lithium-metal batteries.* Sci. Bull. **66.17** (2021): 1746-1753.

36. Ruan, Yadong, et al. *A 3D cross-linking lithiophilic and electronically insulating interfacial engineering for garnet-type solid-state lithium batteries.* Adv. Funct. Mater. **31.5** (2021): 2007815.

37 Park, Richard J-Y., et al. *Semi-solid alkali metal electrodes enabling high critical current densities in solid electrolyte batteries.* Nat. Energy **6.3** (2021): 314-322.

38 Wan, Zipei, et al. *Three-dimensional alloy interface between $Li_{6.4}La_3Zr_{1.4}Ta_{0.6}O_{12}$ and Li metal to achieve excellent cycling stability of all-solid-state battery.* J. Power Sources **505** (2021): 230062.

39. He, Xia, et al. *Cu-Doped Alloy Layer Guiding Uniform Li Deposition on a Li–LLZO Interface under High Current Density.* ACS Appl. Mater. Interfaces **13.35** (2021): 42212-42219.

40. Zhong, Yiren, et al. *A Highly Efficient All-Solid-State Lithium/Electrolyte Interface Induced by an Energetic Reaction.* Angew. Chem. Int. Ed **59.33** (2020): 14003-14008.

41 Hitz, Gregory T., et al. *High-rate lithium cycling in a scalable trilayer Li-garnet-electrolyte architecture.* Mater. Today **22** (2019): 50-57.

42. Kazyak, Eric, et al. *Li penetration in ceramic solid electrolytes: operando microscopy analysis of morphology, propagation, and reversibility.* Matter **2.4** (2020): 1025-1048.

43. Han, Fudong, et al. *High electronic conductivity as the origin of lithium dendrite formation within solid electrolytes.* Nat. Energy **4.3** (2019): 187-196.

44. Porz, Lukas, et al. *Characterizing brittle fracture by modeling crack deflection angles from the microstructure* J. Am. Ceram. Soc. **98.12** (2015): 3690-3698.

45. Cheng, Eric Jianfeng, Asma Sharafi, and Jeff Sakamoto. *Intergranular Li metal propagation through polycrystalline $Li_{6.25}Al_{0.25}La_3Zr_2O_{12}$ ceramic electrolyte.* Electrochim. Acta **223** (2017): 85-91.

46. Lewis, John A., et al. *Chemo-mechanical challenges in solid-state batteries.* Trends Chem. **1.9** (2019): 845-857.

47. Wang, Haifeng, et al. *TEM study of electrochemical cycling-induced damage and disorder in $LiCoO_2$ cathodes for rechargeable lithium batteries.* J. Electrochem. Soc. **146.2** (1999): 473.

48. Yu, Seungho, and Donald J. Siegel. *Grain boundary softening: a potential mechanism for lithium metal penetration through stiff*

solid electrolytes. ACS Appl. Mater. Interfaces **10.44** (2018): 38151-38158.

49. Vishnugopi, Bairav S., et al. *Mesoscale Interrogation Reveals Mechanistic Origins of Lithium Dendrites along Grain Boundaries in I.* Adv. Eng. Mater. **12.3** (2022).

50. Yılmaz, Isık. *Gypsum/anhydrite: some engineering problems.* Bull. Eng. Geol. Environ. **60.3** (2001): 227-230.

51. Usiskin, Robert E., and Joachim Maier. *Guidelines for optimizing the architecture of battery insertion electrodes based on the concept of wiring lengths.* Phys. Chem. Chem. Phys. **20.24** (2018): 16449-16462.

AUTHOR CONTRIBUTIONS

D.R., V.R., and F.F. performed the experimental work. SG synthesized the single crystals, YMC and CF performed finite element calculations. D.R. supervised the work. D.R., J.F., V.R., and F.F. wrote the first draft of the manuscript. All authors contributed to the final draft.

COMPETING INTERESTS

The authors declare no competing interests.